Earth and Planetary Science Letters 412 (2015) 112–121

Contents lists available at ScienceDirect

Earth and Planetary Science Letters

www.elsevier.com/locate/epsl

Potential Antarctic Ice Sheet retreat driven by hydrofracturing and ice cliff failure

David Pollard [a,*], Robert M. DeConto [b], Richard B. Alley [a,c]

[a] Earth and Environmental Systems Institute, 2217 Earth-Engineering Science Building, Pennsylvania State University, University Park, PA 16802, USA
[b] Department of Geosciences, University of Massachusetts, Amherst, MA 01003, USA
[c] Department of Geosciences, Pennsylvania State University, University Park, PA 16802, USA

ARTICLE INFO

Article history:
Received 31 July 2014
Received in revised form 12 December 2014
Accepted 14 December 2014
Available online 6 January 2015
Editor: G.M. Henderson

Keywords:
ice sheet
Antarctica
sea level
subglacial basin
ice cliff
hydrofracture

ABSTRACT

Geological data indicate that global mean sea level has fluctuated on 10^3 to 10^6 yr time scales during the last ~25 million years, at times reaching 20 m or more above modern. If correct, this implies substantial variations in the size of the East Antarctic Ice Sheet (EAIS). However, most climate and ice sheet models have not been able to simulate significant EAIS retreat from continental size, given that atmospheric CO_2 levels were relatively low throughout this period. Here, we use a continental ice sheet model to show that mechanisms based on recent observations and analysis have the potential to resolve this model–data conflict. In response to atmospheric and ocean temperatures typical of past warm periods, floating ice shelves may be drastically reduced or removed completely by increased oceanic melting, and by hydrofracturing due to surface melt draining into crevasses. Ice at deep grounding lines may be weakened by hydrofracturing and reduced buttressing, and may fail structurally if stresses exceed the ice yield strength, producing rapid retreat. Incorporating these mechanisms in our ice-sheet model accelerates the expected collapse of the West Antarctic Ice Sheet to decadal time scales, and also causes retreat into major East Antarctic subglacial basins, producing ~17 m global sea-level rise within a few thousand years. The mechanisms are highly parameterized and should be tested by further process studies. But if accurate, they offer one explanation for past sea-level high stands, and suggest that Antarctica may be more vulnerable to warm climates than in most previous studies.

1. Introduction

Studies of sea-level variations over the last ~25 million years include geochemical and faunal analysis of ocean core records, and paleo-shoreline indicators, indicating quite high stands at some times (Miller et al., 2012; Foster and Rohling, 2013; Naish and Wilson, 2009; Raymo and Mitrovica, 2012). There is some uncertainty about how much their high-stand values are distorted regionally by glacial isostatic adjustment and dynamic topography (Rowley et al., 2013; Rovere et al., 2014). Here we assume that some of them do represent eustatic high stands at least 20 m above modern, which could only have been caused by ice loss from Greenland and Antarctica.

Most of the West Antarctic Ice Sheet (WAIS) is grounded well below sea level, with extensive grounding lines and wide ice shelves directly in contact with the ocean. Models and data indicate this ice is vulnerable to ocean warming, and has probably collapsed and recovered multiple times in the past (Vaughan, 2008; Naish et al., 2009). Increased oceanic melting at the base of floating ice shelves causes thinning and reduces their buttressing effect (back stress) on interior ice, and if the bed deepens upstream, this can lead to runaway retreat due to the very strong dependence of ice flux on grounding-line depth – termed "Marine Ice Sheet Instability" (MISI) (Weertman, 1974; Mercer, 1978; Schoof, 2007). However, the contribution of a complete marine WAIS collapse to global sea level is only ~3.3 m above modern (Bamber et al., 2009). The Greenland Ice Sheet, after its first full growth probably in the Pliocene, also diminished considerably during past warm interglacial periods (mainly by surface melting due to its lower latitudes), but contributed perhaps as little as ~2 m to global sea level during the last interglacial (Dahl-Jensen et al., 2013), and at most ~7.3 m if complete collapse occurred during earlier warm times (Alley et al., 2010). Together, WAIS and later Greenland have contributed at most ~3 to 10 m, so past sea-level variations of 20 m or more above modern require East Antarctic contributions of at least 10 to 17 mesl (meters equivalent sea level), ~20 to 30% of its modern volume.

* Corresponding author. Tel.: +1 814 865 2022.
E-mail address: pollard@essc.psu.edu (D. Pollard).

http://dx.doi.org/10.1016/j.epsl.2014.12.035

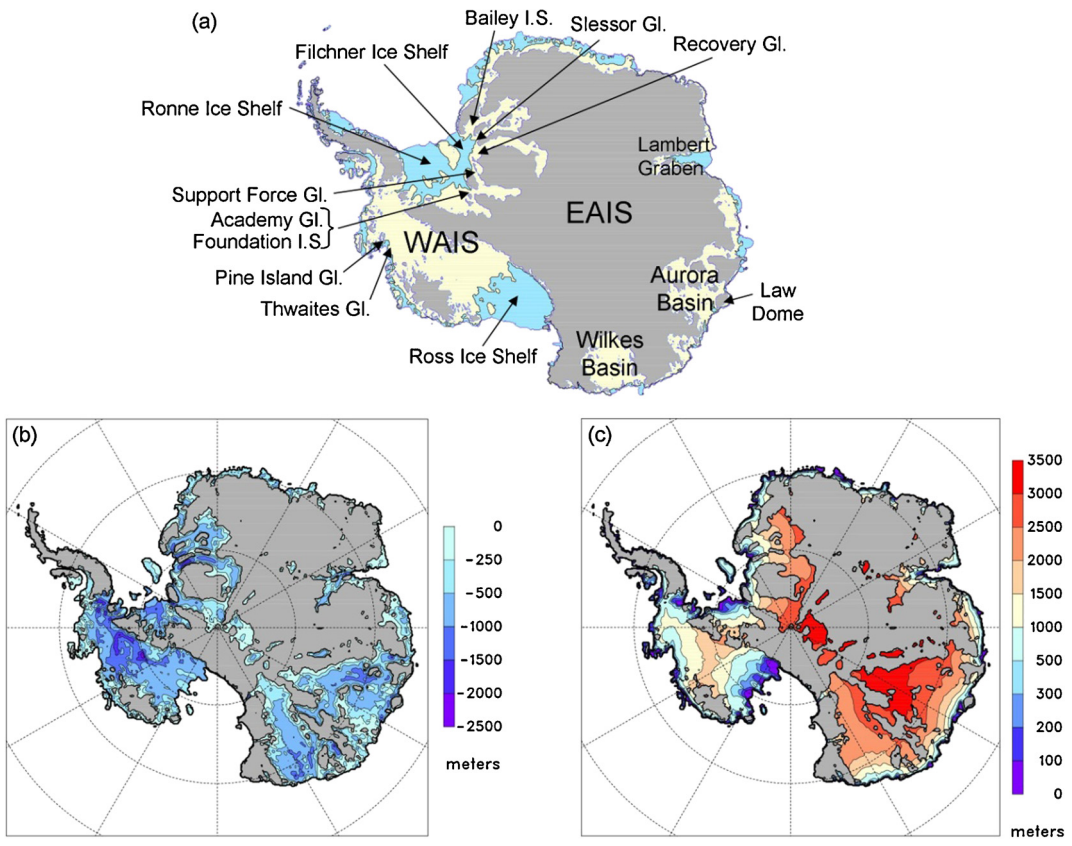

Fig. 1. Antarctic location map and modern properties. (a) Locations of features named in the text. EAIS = East Antarctic Ice Sheet, WAIS = West Antarctic Ice Sheet, I.S. = ice stream, Gl. = glacier. Yellow shading shows the areas of grounding line retreat after 5000 yr in the main retreat simulation of Fig. 3, and cyan areas are modern floating ice shelves. (b) Modern bedrock elevations that are below sea level. (c) Modern ice thickness above flotation, i.e., $h_i - (\rho_w/\rho_i)(S - h_b)$ where h_i is ice thickness, h_b is bed elevation, S is sea level, and $\rho_w/\rho_i = 1028/910$ is the ratio of ocean to ice densities used in the model. h_i and h_b are regridded to 10 km from the Bedmap2 dataset (Fretwell et al., 2013). Values are shown only for ice grounded below sea level (where $h_b < S$), highlighting the volume of ice that effectively contributes to sea level rise if melted, *and* is potentially vulnerable to cliff-failure attack. The much greater values in East Antarctica compared to West explain why the EAIS contribution to sea-level rise in our simulations is larger, despite its similar area of collapse to WAIS.

In contrast to WAIS, most of the EAIS is grounded above sea level and is not directly vulnerable to ocean warming. The EAIS first attained full continental size at the Eocene–Oligocene boundary (Pusz et al., 2011; DeConto and Pollard, 2003). The atmospheric warming necessary to produce substantial retreat from continental size in previous ice-climate model simulations is considerable, ~15 to 20 °C (Huybrechts, 1993) or atmospheric CO_2 levels of ~4× to 9× PAL (Preindustrial Atmospheric Level, 280 ppmv) (Pollard and DeConto, 2005). Higher-resolution climate model simulations with ~2× PAL CO_2 predict very little surface melting of East Antarctica except on narrow strips around the margins, and no overall retreat; in fact, the EAIS volume *increases* due to greater snowfall in the warmer atmosphere for CO_2 up to 2× PAL (Vizcaino et al., 2010; Ligtenberg et al., 2013). This behavior is well understood, and stems from hysteresis between climate and equilibrium Antarctic ice sheet size, with the steep ice-sheet flanks and atmospheric lapse rate protecting most of the surface from warming summer temperatures (Height–Mass-Balance Feedback; Huybrechts and de Wolde, 1999; Oerlemans, 2002). Given proxy records of CO_2 of only 1 to 2× PAL since the late Oligocene (Pagani et al., 2005; Beerling and Royer, 2011), these results rule out substantial EAIS retreat due directly to surface mass loss.

East Antarctica has several large sub-glacial basins with beds well below sea level (Wilkes, Aurora, and groups on the eastern side of the Filchner–Ronne ice shelves being the largest; Fig. 1). Although generally not as deep and wide as in West Antarctica, these basins all have grounding lines in contact with the modern ocean at depths of hundreds of meters, and beds deepening upstream to ~1 km or more below sea level with the potential for marine instabilities. The combined ice volume above flotation in these basins is equivalent to ~15 to 20 mesl, which could account for the inferred Cenozoic sea level variability.

In most prior 3-D ice-sheet models with some representation of marine physics (Ritz et al., 2001; Huybrechts, 2002; Pollard and DeConto, 2009; Nowicki et al., 2013), WAIS retreats drastically in past and future warm climates, but grounding lines in East Antarctic basins retreat only slightly from modern positions even with substantial ocean warming. Presumably this is because East Antarctic basins have shallower and narrower sills at modern grounding lines, greater buttressing by floating ice in the narrower embayments, and frozen or stiffer beds. However, two recent studies (Fogwill et al., 2014; Mengel and Levermann, 2014) have produced significant retreat in some East Antarctic basins due to oceanic warming with the PISM ice-sheet model, suggesting some model dependency in this behavior. East Antarctic basin retreat is also found in a recent model intercomparison study for the Pliocene, but may be dependent on the imposed initial conditions (de Boer et al., 2014, and interactive discussion). These models use simplified or hybrid treatments of ice dynamics (e.g., Pollard and DeConto, 2012), and it would be desirable to confirm the behavior with higher-order dynamical treatments, but simulations with such models are currently feasible only on smaller scales, and model intercomparisons to date (in which hybrid models have generally performed well) have been confined to idealized geometries (Pattyn et al., 2013).

In this study we assume that additional physical processes are needed to produce East Antarctic retreat. We add two mechanisms to an established Antarctic ice-sheet model, namely hydrofracturing by surface water, and large ice-cliff failure, and perform simulations with climate representative of past warm periods. Our parameterizations of these mechanisms are based on previous work and observations, but are new to this type of model. The ice-sheet model, mechanisms, and climate forcing are described briefly below, and in more detail in Appendices A and B and Supplementary Material.

2. Methods

2.1. Ice sheet model

The 3-D ice-sheet model is described further in Supplementary Material (Section S.1) and Pollard and DeConto (2012). It has previously been applied to past Antarctic variations in Pollard and DeConto (2009) and DeConto et al. (2012). The model predicts ice thickness and temperature distributions over the Antarctic continent, evolving due to slow deformation under its own weight, and to mass addition and removal (precipitation, basal melt and runoff, oceanic melt, calving of floating ice, and cliff failure described below). Floating ice shelves and grounding-line migration are included. It uses hybrid ice dynamics and an internal condition on ice velocity at the grounding line (Schoof, 2007). Bedrock deformation is modeled as an elastic lithospheric plate above local isostatic relaxation. A grid size of 10 km is used for all runs in the main paper, the finest resolution for which long-term continental simulations are computationally feasible.

2.2. Structural failure at the grounding line

We apply a recently proposed mechanism (Bassis and Walker, 2012; Bassis and Jacobs, 2013) to the ice-sheet model, that can cause drastic grounding-line retreat into the major EAIS basins. There is presumably a maximum height of vertical ice cliffs above the ocean surface at the grounding lines of tidewater glaciers and ice sheets, beyond which tensile or shear stresses at the ice face, due simply to the unbalanced overburden of ice above, exceed the yield strength of ice causing the cliff to fail catastrophically. The largest vertical subaerial ice cliffs observed today are approximately 100 m high, e.g., Jakobshavn Isbrae and Helheim glaciers in Greenland (Nick et al., 2013; James et al., 2014), and Crane glacier in the Antarctic Peninsula after Larsen B breakup (Scambos et al., 2011). Consistently, Bassis and Walker (2012) analytically estimate the maximum ice cliff size at flotation (ice and water columns of equal weight) to be ∼100 m, for parameter ranges that best fit empirical data. Hanson and Hooke (2003) reach similar conclusions.

Bassis and Walker's vertically averaged force analysis and failure criterion apply equally to tidewater cliffs and to grounding lines with unbuttressed ice shelves (i.e., free floating shelves with no lateral drag, compression or pinning points to provide back stress). This is because the vertically integrated hydrostatic force imbalance at the grounding line that must be compensated by longitudinal stresses (along-flow stretching) is exactly the same for a tidewater cliff at flotation as it is for an unbuttressed ice shelf. Consequently, structural failure in our model can occur both at tidewater faces with tall subaerial cliffs, and at deep grounding lines with free-floating ice shelves. For brevity we refer to both as "cliff failure", short for "structural failure at the grounding line". Our formulation is described in detail in Appendix A.

2.3. Hydrofracture due to surface melt

To trigger cliff failure, floating ice must first be removed, either entirely or at least enough to greatly reduce back pressure at the grounding line. Even very rapid melting from oceanic heat is often slower than ice-stream velocities, and is usually insufficient on its own to sufficiently reduce the major ice shelves in our model. We apply an additional mechanism accounting for increased ice-shelf calving due to hydrofracture by surface melt and rainfall draining into crevasses (Nick et al., 2013). Surface melting has been strongly implicated in the recent breakup of the Larsen B ice shelf (Scambos et al., 2003). In our warm-climate scenarios, surface melting increases calving considerably around the Antarctic margins. Our treatment of calving including hydrofracturing is described in Appendix B.

As well as increasing calving of floating ice, melt-driven hydrofracturing also deepens surface crevasses in the immediate vicinity of the grounding line, which weakens the ice column. The vertical-mean force-balance analysis used to predict cliff failure at the grounding line already takes dry surface crevassing into account (Bassis and Walker, 2012); here the analysis is extended to account for weakening due to hydrofractures, and also for strengthening due to ice-shelf buttressing (see Appendix A). In our warm climates, hydrofracture-induced weakening at the grounding line can cause cliff failure at considerably smaller column heights than with no hydrofracturing (i.e., less than ∼900 m total ice thickness, ∼100 m subaerial cliff if no ice shelf). This concept is basically consistent with widespread crevassing on modern temperate tidewater glaciers (Meier and Post, 1987).

2.4. Combined hydrofracture and cliff failure

Today, cliff failure in Antarctica is prevented by (1) grounding lines at basin sills not being deep enough ($<$ ∼800 m), (2) insufficient surface melt to cause hydrofracturing and weakening at the grounding line, and/or (3) buttressing at the grounding lines by major ice shelves. In our warm-climate simulations, a combination of increased sub-ice ocean melt (reducing buttressing) and hydrofracturing (reducing buttressing and weakening grounding-line columns) leads to cliff failure in the major basins (Fig. 2). For deep basins, this sequence proceeds catastrophically, until either (i) surface melting and hydrofracturing lessen, strengthening ice columns at the grounding line, (ii) normal deformational ice flow across the grounding line exceeds calving and ocean melting, so that a substantial ice shelf re-forms and provides buttressing at the grounding line, or (iii) the grounding line retreats to the inner part of the basin with beds shallower than ∼800 m and little ice above flotation.

Our implementation of these processes is described in Appendices A, B. The cliff-failure parameterization represents net wastage from the entire ice column, and does not attempt to capture details such as the timing or mode of individual fracture events, which probably have no analog in the modern world. Huge calving events observed at the fronts of Jakobshavn Isbrae and Helheim glaciers (Amundson et al., 2010; James et al., 2014), in water depths of ∼700 m to 1000 m with no contiguous ice shelves, may be the closest example, but may still not be a good analog as discussed in Appendix A.

3. Results: warm climate forcing

To investigate the impact of the cliff-failure and melt-driven hydrofracture mechanisms, the ice-sheet model is run forward in time, forced by climate representative of past warm periods. Simulations are started from a previous spin-up of modern Antarctica using observed climatology. An instantaneous change to a warmer climate is applied, broadly representative of a warm Pliocene period. The past warm atmospheric climate is obtained from the RegCM3 Regional Climate Model (Pal et al., 2007) applied over Antarctica with some physical adaptations for polar regions, and

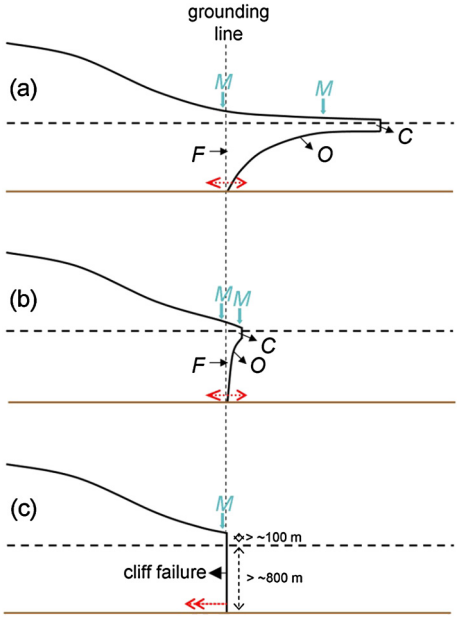

Fig. 2. Schematic cross-sections of an ice sheet approaching cliff failure. Ice flow is from left to right, from grounded ice to floating shelf. M = surface liquid runoff into crevasses. C = calving. O = oceanic basal melt. F = deformational flow across the grounding line. Red arrows show possible grounding-line movement. (a) With substantial ice shelf, and shallow surface slopes in the grounding zone. (b) After strong warming (large M, C, O) with the shelf nearly removed but still allowing shallow slopes. (c) With the shelf completely removed, exposing a vertical cliff $> \sim 100$ m above sea level that undergoes structural failure, causing very rapid grounding-line retreat. Note that "cliff" failure can also occur at grounding lines with ice shelves, if the ice shelf provides little or no buttressing. It can occur in shallower depths than shown if the ice column at the grounding line is weakened by melt-driven hydrofracturing M (see text).

with 400 ppmv CO_2 and an orbit yielding particularly strong austral summers (DeConto et al., 2012). Detailed simulation of ocean warming beneath Antarctic ice shelves is currently not feasible on these time scales, so a simple uniform increment of +2 °C is added to modern observed ocean temperatures, broadly consistent with circum-Antarctic warming in Pliocene paleo-oceanic reconstructions (Dowsett et al., 2009). The climate forcings are described in more detail in Supplementary Material Section S.3.

Fig. 3 shows that the new mechanisms cause retreat deep into the major East Antarctic basins within a few thousand years. As expected from previous modeling (Pollard and DeConto, 2009), the West Antarctic marine ice collapses first. It would collapse without the new mechanisms due to MISI, but here the WAIS retreat is greatly accelerated by the new mechanisms, occurring on decadal rather than century-to-millennial time scales. Retreat into the Wilkes basin and Recovery–Slessor–Bailey system begins after their ice shelves are melted, and is well under way after a few hundred years. There is also relatively minor retreat in the Support Force-Academy-Foundation group, and in the Lambert Graben. In the Aurora sector, bedrock depths around the coastal periphery are shallower (~500 m; Roberts et al., 2011), so cliff failure proceeds at a slower rate for the first ~2000 years. After that, grounding lines retreat into the deeper interior Aurora basin, accelerating cliff failure and producing basin-wide collapse within ~5000 model years.

After ~5000 yr the lagged bedrock rebound due to the reduced ice load in the collapsed basins becomes significant. Rising bedrock topography in the Wilkes and Aurora basins allows numerous small islands to emerge, and grounding lines re-advance slightly, reflected also in equivalent sea level (Supplementary Material Fig. S4a, red curve). In the Aurora basin, some areas of ice-free land become exposed, and remain ice-free for the remainder of the simulation due to strong summer surface melt (Fig. 3h).

The equivalent eustatic sea level rise reaches 5 m after ~200 yr and 17 m after ~3000 yr (Fig. 4, red curve), similar in magnitude to albeit uncertain proxy estimates of past sea-level variations mentioned above. About 3 mesl comes from West Antarctica, and the remaining ~14 mesl comes from East Antarctic basins. The bigger contribution of EAIS, despite its similar area of collapse to

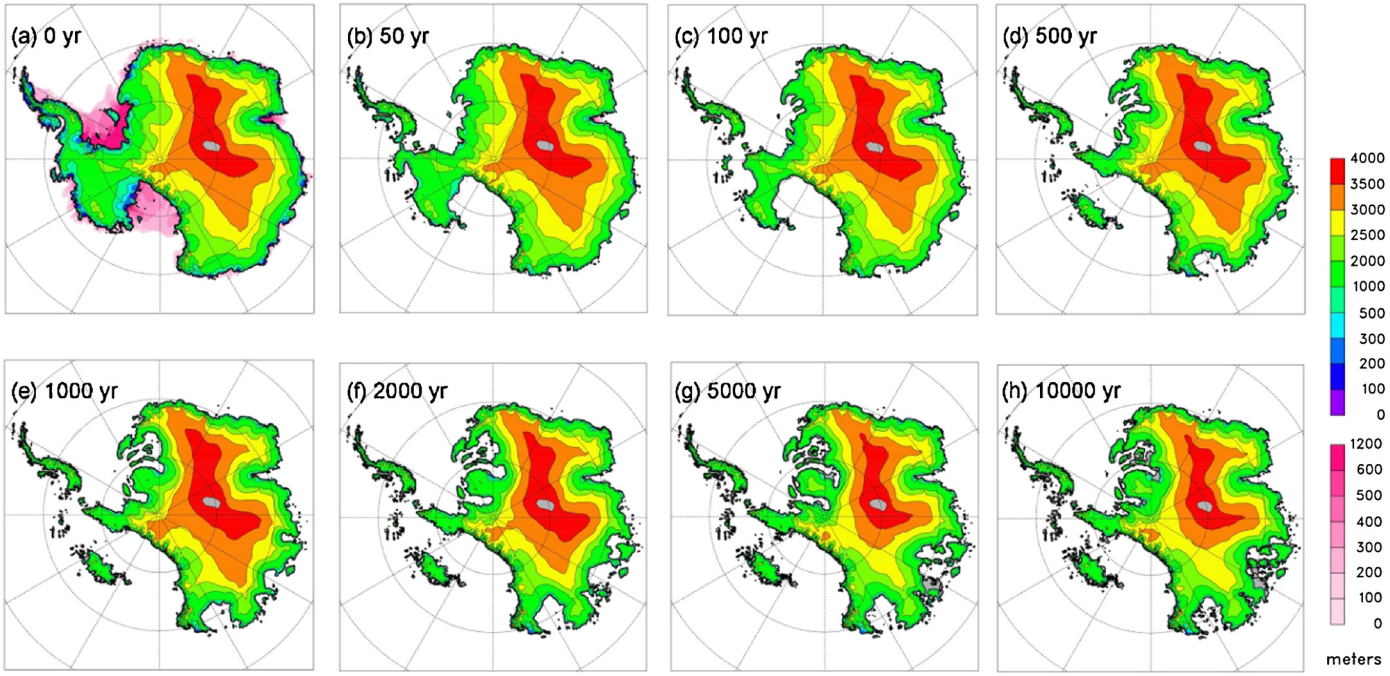

Fig. 3. Ice distributions in a warm-climate simulation. The simulation starts from modern conditions, with a step-function change to a generic past warm climate applied at year 0. Atmospheric temperatures and precipitation are from a Regional Climate Model simulation with hot austral summer orbit, CO_2 = 400 ppmv, and ocean temperatures are increased uniformly by 2 °C above modern. Color scale: Grounded ice elevations, m. Pink scale: floating ice thicknesses, m. The run is initialized from a previous simulation equilibrated to modern climate (panel (a), 0 yr). Both new mechanisms (cliff failure and melt-driven hydrofracturing) are active.

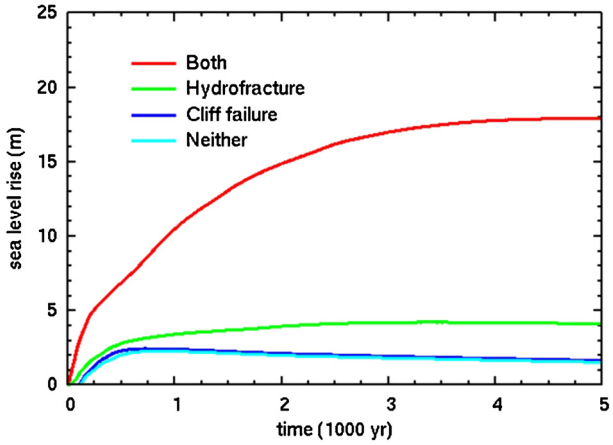

Fig. 4. Global mean equivalent sea level rise in warm-climate simulations. Time series of global mean sea level rise above modern are shown, implied by reduced Antarctic ice volumes. The calculation takes into account the lesser effect of melting ice that is originally grounded below sea level. *Cyan:* with neither cliff failure nor melt-driven hydrofracturing active. *Blue:* with cliff failure active. *Green:* with melt-driven hydrofracturing active. *Red:* with both these mechanisms active. Geographic ice distributions for the latter run are shown in Fig. 3, and for the other runs in Fig. 5.

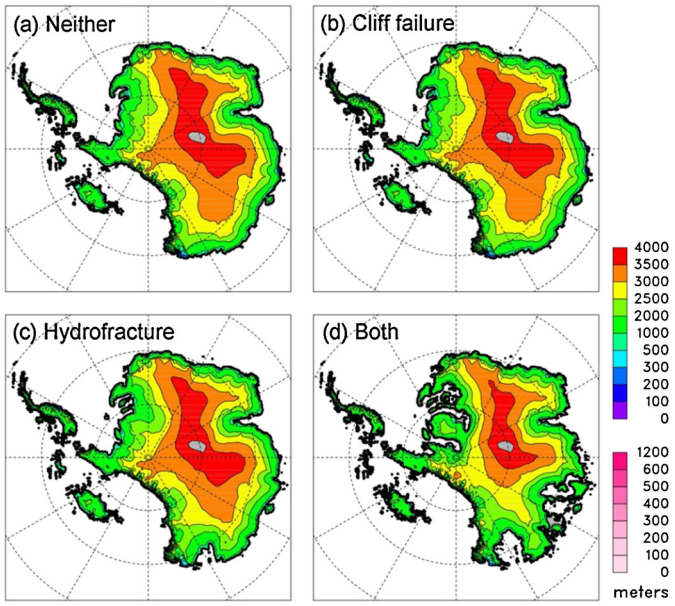

Fig. 5. Ice distributions with different combinations of retreat mechanisms. Equilibrated states are shown after 5000 yr of warm-climate forcing. (a) With neither cliff-failure nor melt-driven hydrofracturing active. (b) With cliff failure active. (c) With melt-driven hydrofracturing active. (d) With both these mechanisms active.

WAIS, is explained by the much greater volumes of ice above flotation in the East Antarctic basins, particularly in the Aurora (Fig. 1c).

4. Roles of individual mechanisms

We first note that in modern simulations (Fig. 3a, Supplementary Material Fig. S5a, top row), the total amounts of basal ice melt and calving for all Antarctica are close to equal (∼1100 and 1300 gigatons per year respectively, or ∼0.08 and 0.10 $\mathrm{m\,a^{-1}}$ averaged over all ice area), in rough agreement with recent observational estimates (Depoorter et al., 2013; Rignot et al., 2013). Total removal by the cliff failure mechanism is negligible in modern simulations.

The individual contributions of the new mechanisms can be assessed by re-running the simulation with cliff failure and/or melt-driven hydrofracturing turned on or off, as shown by the sea-level curves in Fig. 4, and maps in Fig. 5. With both mechanisms turned off (Fig. 5a), the model functions much as in earlier work (Pollard and DeConto, 2009). As expected, West Antarctica undergoes major collapse driven primarily by increased sub-ice melt from the +2 °C ocean warming, causing reduced buttressing at the major WAIS grounding lines, and leading to classic marine instability (MISI) into the deepening interior beds (Weertman, 1974; Schoof, 2007). The time scale of this retreat is several hundred to a thousand years (Pollard and DeConto, 2009, and Fig. 4, cyan curve). There is very minor grounding-line recession into the outer Slessor–Bailey troughs and Lambert Graben due to ice-shelf thinning and reduced buttressing, but the retreat stops, presumably due to greater side-drag and funneling of ice compared to the wider West Antarctic grounding zones. Similar minor retreat occurs in a few other East Antarctic locations, but nothing on the scale of the retreat in Fig. 3. The same is true if cliff failure is active alone (without hydrofracturing, Fig. 5b), because ice shelves still exist, which buttress grounding lines and prevent cliff failure. With hydrofracturing activated alone (without cliff failure, Fig. 5c), the drastic removal of floating ice further reduces buttressing, allowing MISI to produce partial retreat into the Wilkes and Recovery–Slessor–Bailey basins, but not into the shallower Aurora. Full collapse into all basins, and greatly accelerated collapse in West Antarctica, requires the combination of melt-driven hydrofracturing and cliff failure (Fig. 5d). More analysis on the roles of the individual retreat mechanisms, and other sensitivities and basic model tests, are included in Supplementary Material Sections S.4–S.7.

5. Summary and discussion

In summary, applying a simple Pliocene-like warming scenario to our model, the combined mechanisms of MISI, melt-driven hydrofracturing and cliff failure cause a very rapid collapse of West Antarctic ice, on the order of decades. This is followed by retreat of East Antarctic basins within several hundred to a few thousand years. The total Antarctic ice loss corresponds to ∼+17 m sea-level rise, in good agreement with high stands in geologic sea-level records, although uncertainty in the geologic records themselves should be considered (Rowley et al., 2013; Rovere et al., 2014).

For simplicity, this paper uses step-function climate forcing representative of generalized warming episodes during the late Cenozoic. A natural next step will be to use time-dependent forcing to model specific warm events or periods of the past and compare with available data, such as warm Pliocene intervals ∼5–3 Ma, MIS-31 at ∼1.08 Ma, and strong Pleistocene interglacials (Naish et al., 2009; Raymo and Mitrovica, 2012; O'Leary et al., 2013). Another important step will be the use of regional ocean models to resolve different oceanic responses in different Antarctic embayments (Hellmer et al., 2012). Results for specific times can be compared with local geologic evidence of past East Antarctic retreats (Williams et al., 2010; Young et al., 2011; Cook et al., 2013; Patterson et al., 2014).

The main aim of adding hydrofracturing and cliff failure was to produce total Antarctic retreat consistent with albeit poorly constrained past sea-level data, and no effort was made to adjust the rate of retreat. The time scale that emerges for West Antarctic collapse (∼3 m contribution to global sea-level rise within $O(100)$ years after a step-function warming) is an order of magnitude faster than previous estimates for the next century, which range from ∼0.1 to 0.6 m by 2100 AD (Pfeffer et al., 2008; Levermann et al., 2014; Joughin et al., 2014). The modeling approaches in Pfeffer et al. and Levermann et al. are very different, and our study is not directly applicable to the future because of our step-function

climate change, Pliocene-like climate, and homogeneous ocean warming. But even so, our predicted WAIS retreat rates are much faster than might be expected from the previous work. The main cause is the new mechanisms of hydrofracture and cliff failure.

It should be emphasized that these mechanisms are highly parameterized in our model and are somewhat speculative. On the one hand, it seems likely that in reality (i) substantial surface melting occurs around Antarctic peripheries in warmer-than-present climates (some is already occurring today), and (ii) if there is enough surface water to cause complete disintegration of Antarctic ice shelves, then cliff failure could well occur at major grounding lines, perhaps similarly to Jakobshavn, Helheim and Crane Glaciers today. On the other hand, the results presented here depend on uncertain parameter values, for instance the quadratic relationship between surface water and hydrofracturing (Eq. (B.6)), which asserts that surface melt rates of ∼2 (3) m a^{-1} cause hydrofracturing to a depth of 400 (900) m, and would guarantee disintegration of ice shelves of that thickness or less. Both the hydrofracturing and cliff-failure parameterizations should be tested in further process studies.

There are additional uncertainties in the current model. Grounding-line behavior in hybrid ice-sheet models is sensitive to model details (Nowicki et al., 2013; Fogwill et al., 2014; Mengel and Levermann, 2014), and the results should be tested with higher-order dynamical treatments (Pattyn et al., 2013; Favier et al., 2014) as they become computationally feasible on these spatial and temporal scales. Also, this preliminary study does not include several feedback processes that could reduce the drastic retreat rates found here, such as clogging of seaways by ice mélange, and ice–ocean gravitational interaction (see Supplementary Material Section S.8). But if the geologic sea-level data and our model simulations are even approximately realistic, the mechanisms described here offer an explanation for past high sea-level stands, and suggest that East Antarctic subglacial basins may be more vulnerable than in most previous models.

Acknowledgements

We thank two anonymous reviewers and Anders Levermann for their thoughtful reviews. This research was funded by the National Science Foundation under awards ANT 1043018 (D.P.), OCE 1202632, AGS 1203910/1203792 (R.D., D.P.), ANT 0424589 (R.A., D.P.), and by the National Aeronautics and Space Administration under award NNX-10-AI04G (R.A.).

Appendix A. Ice structural failure parameterization

A large literature exists with detailed viscoelastic modeling of stresses and fracture patterns at the vertical calving faces of modern tidewater glaciers (reviewed in Benn et al., 2007), but to our knowledge only a few papers address a maximum-height structural limit – Hanson and Hooke (2003), and explicitly Bassis and Walker (2012) and Bassis and Jacobs (2013) as discussed above and below. Reeh (1968) approached it to some extent with basic mechanical modeling, and provides tables of maximum shear stress associated with different cliff heights (his Table III; although the largest total ice thickness considered is 800 m).

Our parameterization is based on Bassis and Walker's (2012) vertical mean force balance analysis at the grounding line. As in Bassis and Walker, it applies equally to tidewater cliffs and to grounding-line ice columns with an unbuttressed ice shelf (i.e., no lateral drag, compression or pinning points). For brevity, we refer to structural failure in both situations as "cliff failure". The analysis is extended below to allow for back stress (buttressing) by ice shelves, and for weakening in the grounding-line vicinity by hydrofracturing due to melt or rain draining into surface crevasses. Buttressing reduces longitudinal stress at the grounding line, and also decreases the depth of dry crevasses, which tend to prevent cliff failure. Hydrofracturing increases the depth of surface crevasses, which tends to increase cliff failure. Both of these processes enter via a multiplicative factor in the effective grounding-line ice height, which is compared with a maximum height that depends on the yield strength of ice (Eq. (A.3)).

For dry surface crevassing (no hydrofracturing) and no ice shelf, the maximum subaerial cliff height is ∼100 m, using an ice yield strength of 1 MPa and zero coefficient of friction, which are uncertain but found to best fit empirical tidewater glacier data (Bassis and Walker, 2012). Notably, maximum subaerial tidewater cliff sizes observed today are not much larger than ∼100 m; the cliff at Jakobshavn is a few 10's m greater than 100 m in places, but may be partially supported by back stress from the glacier sides or its ice mélange, and so may be slightly higher than the maximum for much wider scales.

The exact mode of failure is not important for this study. The closest analog today might be the separation and overturning of km-scale bergs as observed currently at Jakobshavn and Helheim glaciers (Amundson et al., 2010), perhaps involving buoyant flexure (James et al., 2014). For subaerial cliffs with no ice shelves, it might involve fracturing and violent seaward expelling of ice near the water line (the rough location of maximum unbalanced hydrostatic stress for tidewater cliffs, Bassis and Walker, 2012) in a process not seen today. Similarly, the frequency of individual brittle failure events, assumed to be fast compared to the ice-sheet model timestep, is not otherwise addressed. The net effect of the failure is expressed in Eq. (A.4) below, as a time-averaged horizontal wastage rate into the vertical ice column, which increases very rapidly as the ice height exceeds a maximum size.

A.1. Formulation

Assuming ice thickness is exactly at flotation at the grounding line (discussed further in Supplementary Material Section S.2.2), the vertical average force balance at the grounding line is:

$$\overline{\tau_{xx}}(h - d_s - d_b - d_w) = \frac{\rho_i g h^2}{2}\left(1 - \frac{\rho_i}{\rho_w}\right)\theta \tag{A.1}$$

where $\overline{\tau_{xx}}$ is the depth-averaged longitudinal stress (in intact non-crevassed ice), h is ice thickness, d_s and d_b are depths of dry-surface and basal crevasses respectively, and d_w is the additional depth of surface crevasses due to hydrofracturing by surface melt and/or rainwater. ρ_i and ρ_w are densities of ice and ocean water respectively, g is gravitational acceleration, and θ is 1 minus the fractional reduction in the hydrostatic imbalance at the grounding line due to back stress on an ice shelf (Schoof, 2007; Pollard and DeConto, 2012). For completely freely floating shelf ice, or no shelf at all, $\theta = 1$, and the right-hand side of Eq. (A.1) is the difference between vertically integrated hydrostatic stress in ice and water columns immediately adjacent to the grounding line.

As discussed in Bassis and Walker, cliff failure occurs if $\overline{\tau_{xx}}$ exceeds a prescribed yield stress of ice τ_c (∼1 MPa, zero coefficient of friction). Re-arranging, this requires

$$\frac{\tau_c}{\rho_i g(1 - \rho_i/\rho_w)} < \frac{h}{2(1 - (d_s + d_b + d_w)/h)}\theta \tag{A.2}$$

Using the Nye (1957) method for dry-surface and basal crevasse depths (longitudinal stress balanced by overburden pressure) with longitudinal stress modified from the free-floating value by factor θ, then $(d_s + d_b)/h = \theta/2$ (as noted for $\theta = 1$ by Bassis and Walker, 2012). Defining a critical ice height above water line $h_c = \tau_c/\rho_i g$ (∼100 m), and assuming no excess ice over flotation at the

grounding line so that $h_s - S = h(1 - \rho_i/\rho_w)$ where h_s is ice surface elevation and S is sea level, then

$$h_c < (h_s - S)\left[\frac{\theta}{2(1-\theta/2 - d_w/h)}\right] \tag{A.3}$$

When the ice above water line $h_s - S$, modified by factors representing back stress and additional wet-crevasse deepening, exceeds the critical height h_c, then cliff failure occurs. This is implemented in the model as a drastic ramp in ice wastage, applied to the grounded ice box adjacent to the grounding line:

$$W = 3000 \max\big[0, \min\big[1, \big((h_s - S)F - h_c\big)/20\big]\big] \tag{A.4}$$

where F is the factor in square brackets on the right-hand side of Eq. (A.3). The deepening of surface crevasses due to hydrofracturing relative to ice thickness, d_w/h, depends on surface melt and rainfall, as in the treatment of calving (Eq. (B.6) below). In practice, $h_s - S$ is set from $h_w(\rho_w/\rho_i - 1)$, where h_w is water depth at the interpolated sub-grid grounding line position (Section 2.3 in Pollard and DeConto, 2012). W (with units of $\mathrm{m\,a^{-1}}$) is equivalent to a horizontal wastage rate of the entire ice column, and its maximum value of 3 $\mathrm{km\,a^{-1}}$ is conservatively based on observations of ice vs. terminus velocities at Jakobshavn Isbrae (Joughin et al., 2012; up to ~12 $\mathrm{km\,a^{-1}}$) and Crane Glacier's terminus retreat (Scambos et al., 2011; ~5 $\mathrm{km\,a^{-1}}$) following recent disintegrations of their ice shelves; the sensitivity of results to other values is examined in Supplementary Material Section S.7.

For numerical convenience in the model dynamics, the wastage W is applied over the entire grid cell surface as if it is a surface balance term, instead of a horizontal wastage rate along one side of the grid box as described above. Hence it is multiplied by ice thickness at the grounding line × cell width / cell area. The calculation is performed for each of the four sides of the affected grid cell, and the wastages are summed. Further numerical aspects are discussed in Supplementary Material Section S2.

Appendix B. Calving parameterization and hydrofracturing

The calving parameterization for floating ice follows and extends Nick et al. (2010, 2013) and others. Depths of surface and basal crevasses are functions of (i) divergence of ice velocity, (ii) accumulated strain, (iii) ice thickness, and (iv) surface liquid water availability. Calving occurs when the combined crevasse depths become comparable to the ice thickness. This parameterization is primarily aimed at tabular floating ice shelves; calving at the vertical faces of small tidewater glaciers (10's m cliff heights; Benn et al., 2007) is not included in the model.

B.1. Dependence on divergence

Large-scale (grid-resolved) extensional stresses are assumed to open crevasses to a depth where the stress is equal to the unbalanced isostatic pressure at the crevasse walls (Nye, 1957; Benn et al., 2007; Nick et al., 2010). Extensional stress is obtained via strain rate and the model SSA rheology. No distinction is made here between along-flow and transverse strains, whose combined effect is represented by ice divergence.

$$d_s = \frac{2}{\rho_i g}\left(\frac{\dot\varepsilon}{A}\right)^{\frac{1}{n}} \tag{B.1a}$$

$$d_b = \left(\frac{\rho_i}{\rho_0 - \rho_i}\right)\frac{2}{\rho_i g}\left(\frac{\dot\varepsilon}{A}\right)^{\frac{1}{n}} \tag{B.1b}$$

where d_s and d_b are depths of dry-surface and basal crevasses respectively, $\dot\varepsilon$ is ice divergence, A is the depth-averaged ice rheological coefficient, $n = 3$ is the rheological exponent, and ρ_i, ρ_w and ρ_o are densities of ice, surface liquid and ocean water respectively. (We first tried using principle strains instead of divergence, as in Levermann et al. (2012), but this produced noisy and erratic results, perhaps due to our relatively coarse model resolution. We have not observed multiple steady ice-shelf states in our runs as found by Levermann et al. (2012), but have not systematically tested for them.)

Calving is potentially applied to all points within the ice shelf, but the setting of divergence $\dot\varepsilon$ depends on whether the floating ice covers all or a fraction of the cell area. A sub-grid parameterization of fractional ice area is used to set an adjusted ice thickness h and fractional cover f_i (Pollard and DeConto, 2012; Albrecht et al., 2011). The treatment is modified slightly from Pollard and DeConto's (2012) Eq. (23), as follows. At the ice-shelf edge adjacent to open ocean, the adjusted thickness h is the average of adjacent interior shelf thicknesses, each multiplied by a "downstream thinning" factor $1 - w(1 - \mathrm{e}^{-\Delta x/100})$ where the weight $w = \min[1, h_u/(h_a \mathrm{e}^{-\Delta x/100})]$, Δx is the grid size in km, h_u is the unadjusted (grid-mean) ice thickness of the edge point, and h_a is the thickness of the adjacent interior point. The weight w is used to force $h \approx h_a$ for small amounts of ice ($h_u \ll h_a$), and to apply more downstream thinning when the edge cell has substantial ice cover. As in Pollard and DeConto (2012), the fractional ice cover of the edge point is set to $f_i = h_u/h$, conserving ice mass.

For interior points (with $f_i = 1$), $\dot\varepsilon$ in Eqs. (B.1) is set to the grid-scale divergence of ice velocity $\partial u/\partial x + \partial v/\partial y$. For edge points (with $f_i < 1$), it is set to the longitudinal spreading value for a freely floating unconfined ice face (e.g., Schoof, 2007), using the adjusted ice thickness h as described above.

$$\dot\varepsilon = \left(\frac{\partial u}{\partial x} + \frac{\partial v}{\partial y}\right) \quad \text{for } f_i = 1 \tag{B.2a}$$

$$\dot\varepsilon = A\left(\frac{\rho_i g h}{4}\right)^n \quad \text{for } f_i < 1 \tag{B.2b}$$

To correct some occasional suspect values of $\partial u/\partial x + \partial v/\partial y$, a condition is imposed that it cannot be greater than the unconfined spreading term in Eq. (B.2b). (Unlike Pollard and DeConto's (2012) Section 2.10, divergence values are *not* propagated from points with $f_i = 1$ to points with $f_i < 1$.)

B.2. Dependence on accumulated strain

As discussed in Bassis and Walker (2012), substituting the unconfined spreading rate in Eq. (B.2b) for $\dot\varepsilon$ in Eqs. (B.1) implies that in dry conditions ($d_w = 0$), the combined crevasse depths $d_s + d_b$ are at most 50% of the ice thickness h. Thus no calving could occur unless the critical crevasse-penetration ratio is set very low (<0.5), or additional crevasse-deepening mechanisms are active (beyond surface liquid drainage described below). There are several such mechanisms, such as higher-order bending stresses and fracture mechanics (Bassis and Walker, 2012, p. 916; Albrecht and Levermann, 2012). Here we use a crude measure of accumulated incipient fractures, proportional to the time integral of large-scale ice divergence along flowlines:

$$\oint \frac{\partial u}{\partial x} dt \tag{B.3a}$$

Assuming steady flow and substituting $dt = dx/(dx/dt) = dx/u$, where u is ice velocity along the flow line, this is equivalent to

$$\oint \frac{\partial \ln(u)}{\partial x} dx = \ln(u_2/u_1) \tag{B.3b}$$

where u_1 and u_2 are flowline velocities at the beginning and end of the trajectory. (Note that these substitutions are only valid for a

reference frame in which the trajectory path is stationary, so the result in Eq. (B.3b) is not independent of a uniform shift in velocities, even though $\partial u/\partial x$ is.) Assuming most incipient fracture generation occurs on floating shelves, an appropriate choice for u_1 is the velocity at the grounding line (typically 10's to 100 $\mathrm{m\,a^{-1}}$ for major shelves) and u_2 is the velocity at any point in question in the shelf.

Although this parameterization is tentative, a dependence on ice velocity would explain the strong calving rates at the fast moving edges of the Ross and Filchner–Ronne shelves, versus much smaller calving rates at the edges of smaller slower-moving East Antarctic ice shelves with similar edge thicknesses. It is implemented here as an additional crevasse deepening d_a (m):

$$d_a = h \max\big[0, \ln(u/1600)\big] / \ln(1.2) \tag{B.4}$$

where h is ice thickness (adjusted as above if at the shelf edge) and u is local ice speed ($\mathrm{m\,a^{-1}}$). d_a is zero for speeds up to 1600 $\mathrm{m\,a^{-1}}$, and approaches h as speeds increase to ∼1900 $\mathrm{m\,a^{-1}}$ and above, as they do in the outer regions of the Ross and Ronne shelves. Eq. (B.4) does not have exactly the same form as Eq. (B.3b) with respect to u and u_2, but has been adjusted pragmatically to yield realistic modern shelf extents for both the major West Antarctic shelves and the smaller shelves fringing the rest of the continent.

Note that the kinematic stretching of crevasses by the grid-resolved divergence $\partial u/\partial x$ is not the issue here, because that would stretch ice thickness equally, without changing the crevasse: thickness ratio. The parameterization represents fine-scale damage caused indirectly by (or at least correlated to) divergence, and subsequent downstream advection.

B.3. Dependence on ice thickness

A pragmatic constraint is imposed for thin floating ice:

$$d_t = h \max\big[0, \min\big[1, (150 - h)/50\big]\big] \tag{B.5}$$

where again h is ice thickness (adjusted as above if at the shelf edge), and d_t is an additional crevasse depth. This simply has the effect of removing floating ice thinner than ∼100 to 150 m, and reduces unrealistic areas of thin ice extending seaward of the modern Ross and Filchner–Ronne calving fronts, where they are not limited by Eq. (B.4). It has the side-effect of not allowing thin ice shelves to grow from small (∼100 m) tidewater glaciers, which may be unrealistic in some cases but does not noticeably affect the large-scale modern and "retreat" simulations here. However, it does reduce the ability of West Antarctic marine ice to regrow following a collapse, as discussed in Supplementary Material Section S.4.

B.4. Dependence on surface liquid water (hydrofracturing)

Surface crevasses containing water are deepened due to the additional opening stress of the liquid by an amount d_w (Benn et al., 2007; Nick et al., 2010, 2013; Cook et al., 2012), where d_w is (ρ_w/ρ_i) times the depth of water drained into the crevasse from mobile surface melt and/or rainfall. d_w (m) is simply set to

$$d_w = 100 R^2 \tag{B.6}$$

where R is the annual surface melt + rainfall available after refreezing ($\mathrm{m\,a^{-1}}$) in the model's surface mass balance scheme. Nick et al. (2013) used a similar expression in their future-Greenland study, but with d_w linearly proportional to R and with coefficients in the range ∼20 to 30. Eq. (B.6) is of course a very rough approximation, representing (i) funneling from the whole ice shelf surface into a much smaller area of crevasses, and (ii) the temporal relationship of liquid input to storage in the crevasses (multi vs. single year) and any intermediate storage or routing in surface lakes and moulins. In reality it could depend on pre-existing and changeable englacial drainage networks (Parizek et al., 2010). In our warm-climate simulations, we find that the coefficient of 100 and the quadratic dependence on R are necessary to produce complete disintegration of ice shelves, which occurs as R values rise above ∼1 to 2 $\mathrm{m\,a^{-1}}$ (somewhat above modern zonal and annual mean mid-latitude rainfall rates). Results for other values of this coefficient are shown in Supplementary Material Section S.7. Throughout the paper, the application of Eq. (B.6) is termed "hydrofracturing", somewhat loosely as other studies have used that term in slightly different ways.

Further modeling and observational studies are needed to better constrain this parameterization. However, the role of surface water in calving is firmly based on process modeling of hydraulic fracturing (Alley et al., 2005), and on observations of the Larsen B ice shelf breakup preceded by surface liquid accumulation (Scambos et al., 2003), with Banwell et al. (2013) suggesting a chain-reaction drainage of supraglacial lakes. Although surface melting and rainfall are minor over much of Antarctica today outside the Peninsula, they are substantial enough near sea level around the East Antarctic margin (Tedesco and Monaghan, 2009; Ligtenberg et al., 2013) to produce numerous supraglacial lakes (Vogel et al., 2013), and their rates become much more significant in our warm-climate simulations. To simplify calibration of the current model, Eq. (B.6) is only applied in the warm-climate experiments, and not in the modern, under the assumption that the limited amount of surface melting around Antarctica to date has not been sufficient to cause significant large-scale ice-shelf calving. This is effectively a bias correction to the model's combined meteorologic prescription/melt scheme/calving parameterization for the present day, with Larsen B regarded as an outlying harbinger of future conditions.

B.5. Combined calving parameterization

The overall calving rate is expressed as a horizontal wastage rate ($\mathrm{m\,a^{-1}}$):

$$C = 3000 \max\big[0, \min\big[1, (r - r_c)/(1 - r_c)\big]\big] \tag{B.7}$$

where r is the ratio of the combined crevasse depths to ice thickness $[d_s + d_b + d_a + d_t + d_w]/h$, and r_c is a critical value for calving onset, set in our experiments to 0.75. In the same way as for cliff failure (Appendix A), for numerical convenience in the model dynamics C is applied over the entire grid cell surface area, so is multiplied by ice thickness h × cell width / cell area. The maximum calving rate of 3 $\mathrm{km\,a^{-1}}$ is somewhat arbitrary. It is reached only during warm-climate retreats, and not in modern simulations where the largest calving rates are ∼1.5 to 2 $\mathrm{km\,a^{-1}}$, balancing ice velocities at the edges of major shelves.

Calving has the potential to suddenly and completely remove the entire ice shelf back to the grounding line if buttressing is lost, since dynamical spreading and associated crevassing increase with thickness, and are greatest at the grounding line in the absence of buttressing (Alley et al., 2008). The floating tongue of Jakobshavn Isbrae collapsed in this way by 2004 after thinning due to warmer ocean water (Joughin et al., 2008), and our current model has the potential to behave in this way because calving can attack both the interior and edges of ice shelves. There is also the potential for calving to cause internal rifts or polynyas surrounded by intact floating ice. This occurs fleetingly during the first ∼20 years after the step-function warm climate is imposed, in narrow coastal strips near the Ross and Filchner–Ronne grounding lines, and as polynyas in smaller shelves. After a few decades nearly all floating ice has disintegrated.

In earlier model versions, calving was suppressed in the confined inner regions of basins, depending on the subtended arc to open ocean (Pollard and DeConto, 2009, 2012). The total arc represented concavity or narrowness of embayments, and the suppression represented back pressure at the calving front by confined mélange (Joughin et al., 2008, 2012; Amundson et al., 2010). Even though this process may play a role in real Antarctic retreats, we feel it is preferable to defer it to future study, rather than use a crude non-physical parameterization with arbitrary effects on the results, especially if it is turned on or off for cool vs. hot climates as in our earlier simulations. It is no longer used here, and, for the same reasons, it is also no longer used to suppress sub-ice oceanic melting, but see discussion in Supplementary Material Section S.4.

Appendix C. Supplementary material

Supplementary material related to this article can be found online at http://dx.doi.org/10.1016/j.epsl.2014.12.035.

References

Albrecht, T., Levermann, A., 2012. Fracture field for large-scale ice dynamics. J. Glaciol. 58, 165–176.

Albrecht, T., Martin, M., Haseloff, M., Winkelmann, R., Levermann, A., 2011. Parameterization for subgrid-scale motion of ice-shelf calving fronts. The Cryo. 5, 35–44.

Alley, R.B., Dupont, T.K., Parizek, B.R., Anandakrishnan, S., 2005. Access of surface meltwater to beds of sub-freezing glaciers: preliminary insights. Ann. Glaciol. 40, 8–14.

Alley, R.B., et al., 2008. A simple law for ice-shelf calving. Science 322, 1344.

Alley, R.B., et al., 2010. History of the Greenland Ice Sheet: paleoclimatic insights. Quat. Sci. Rev. 29, 1728–1756.

Amundson, J.M., et al., 2010. Ice mélange dynamics and implications for terminus stability, Jakobshavn Isbrae, Greenland. J. Geophys. Res. 115, F01005.

Bamber, J.L., Riva, R.E.M., Vermeersen, B.L.A., LeBrocq, A.M., 2009. A reassessment of the potential sea-level rise from a collapse of the West Antarctic Ice Sheet. Science 324, 901–903.

Banwell, A.F., MacAyeal, D.R., Sergienko, O.V., 2013. Breakup of the Larsen B Ice Shelf triggered by chain reaction drainage of supraglacial lakes. Geophys. Res. Lett. 40, 1–5. http://dx.doi.org/10.1002/2013GL057694.

Bassis, J.N., Jacobs, S., 2013. Diverse calving patterns linked to glacier geometry. Nat. Geosci. 6, 833–836.

Bassis, J.N., Walker, C.C., 2012. Upper and lower limits on the stability of calving glaciers from the yield strength envelope of ice. Proc. R. Soc. A, Math. Phys. Eng. Sci. 468, 913–931.

Beerling, D., Royer, D.L., 2011. Convergent Cenozoic CO_2 history. Nat. Geosci. 4, 418–420.

Benn, D.I., Warren, C.R., Mottram, R.H., 2007. Calving processes and the dynamics of calving glaciers. Earth-Sci. Rev. 82, 143–179.

Cook, C.P., et al., 2013. Dynamic behavior of the East Antarctic ice sheet during Pliocene warmth. Nat. Geosci. 6, 765–769.

Cook, S., Zwinger, T., Rutt, I.C., O'Neel, S., Murray, T., 2012. Testing the effect of water in crevasses on a physically based calving model. Ann. Glaciol. 53, 90–96.

Dahl-Jensen, D., et al., NEEM community members, 2013. Eemian interglacial reconstructed from a Greenland folded core. Nature 493, 489–494.

de Boer, B., et al., 2014. Simulating the Antarctic ice sheet in the Late-Pliocene warm period: PLISMIP-ANT, an ice-sheet model intercomparison project. The Cryo. Disc. 8, 5539–5588.

DeConto, R.M., Pollard, D., 2003. Rapid Cenozoic glaciation of Antarctica induced by declining atmospheric CO_2. Nature 421, 245–249.

DeConto, R.M., Pollard, D., Kowalewski, D., 2012. Modeling Antarctic ice sheet and climate variations during Marine Isotope Stage 31. Glob. Planet. Change 88–89, 45–52.

Depoorter, M.A., et al., 2013. Calving fluxes and basal melt rates of Antarctic ice shelves. Nat. Geosci. 502, 89–92.

Dowsett, H.J., Robinson, M.M., Foley, K.M., 2009. Pliocene three-dimensional global ocean temperature reconstruction. Clim. Past 5, 769–783.

Favier, L., et al., 2014. Retreat of Pine Island Glacier controlled by marine ice-sheet instability. Nat. Clim. Change 4, 117–121.

Fogwill, C.J., et al., 2014. Testing the sensitivity of the East Antarctic Ice Sheet to Southern Ocean dynamics: past changes and future implications. J. Quat. Sci. 29, 91–98.

Foster, G.L., Rohling, E.J., 2013. Relationship between sea level and climate forcing by CO_2 on geological timescales. Proc. Natl. Acad. Sci. USA 110, 1209–1214.

Fretwell, P., et al., 2013. Bedmap2: improved ice bed, surface and thickness datasets for Antarctica. The Cryo. 7, 375–393.

Hanson, B., Hooke, R.LeB., 2003. Buckling rate and overhang development at a calving face. J. Glaciol. 49, 577–586.

Hellmer, H., Kauker, F., Timmermann, R., Determann, J., Rae, J., 2012. Twenty-first-century warming of a large Antarctic ice-shelf cavity by a redirected coastal current. Nature 485, 225–228.

Huybrechts, P., 1993. Glaciological modeling of the late Cenozoic East Antarctic Ice Sheet: stability or dynamism? Geogr. Ann. 75A, 221–238.

Huybrechts, P., 2002. Sea-level changes at the LGM from ice-dynamical reconstructions of the Greenland and Antarctic ice sheets during the glacial cycles. Quat. Sci. Rev. 21, 203–231.

Huybrechts, P., de Wolde, J., 1999. The dynamic response of the Greenland and Antarctic ice sheets to multiple-century climatic warming. J. Climate 12, 2169–2188.

James, T.D., Murray, T., Selmes, N., Scharrer, K., O'Leary, M., 2014. Buoyant flexure and basal crevassing in dynamic mass loss at Helheim Glacier. Nat. Geosci. 7, 593–596.

Joughin, I., et al., 2008. Continued evolution of Jakobshavn Isbrae following its rapid speedup. J. Geophys. Res. 113, F04006.

Joughin, I., et al., 2012. Seasonal to decadal scale variations in the surface velocity of Jakobshavn Isbrae, Greenland: observation and model-based analysis. J. Geophys. Res. 117, F02030.

Joughin, I., Smith, B.E., Medley, B., 2014. Marine ice sheet collapse potentially under way for the Thwaites Glacier basin, West Antarctica. Science 344, 735–738.

Levermann, A., Albrecht, T., Wilkelmann, R., Martin, M.A., Haseloff, M., Joughin, I., 2012. Kinematic first-order calving law implies potential for abrupt ice-shelf retreat. The Cryo. 6, 273–286.

Levermann, A., et al., 2014. Projecting Antarctic ice discharge using response functions from SeaRISE ice-sheet models. Earth Syst. Dyn. 5, 271–293.

Ligtenberg, S.R.M., van de Berg, W.J., van den Broeke, M.R., Rae, J.G.L., van Meijgaard, E., 2013. Future surface mass balance of the Antarctic ice sheet and its influence on sea level change, simulated by a regional atmospheric climate model. Clim. Dyn. 41, 867–884.

Meier, M.F., Post, A., 1987. Fast tidewater glaciers. J. Geophys. Res. 92 (B9), 9051–9058.

Mengel, M., Levermann, A., 2014. Ice plug prevents irreversible discharge from East Antarctica. Nat. Clim. Change 4, 451–455.

Mercer, J.H., 1978. West Antarctic ice sheet and CO_2 greenhouse effect: a threat of disaster. Nature 271, 321–325.

Miller, K.G., et al., 2012. High tide of the warm Pliocene: implications of global sea level for Antarctic deglaciation. Geology 49, 407–421.

Naish, T.R., Wilson, G.S., 2009. Constraints on the amplitude of mid-Pliocene (3.6–2.4 Ma) eustatic sea-level fluctuations from the New Zealand shallow-marine sediment record. Philos. Trans. R. Soc. Lond. A 367, 169–187.

Naish, T.R., et al., 2009. Obliquity-paced Pliocene West Antarctic oscillations. Nature 458, 322–328.

Nick, F.M., van der Veen, C.J., Vieli, A., Benn, D.I., 2010. A physically based calving model applied to marine outlet glaciers and implications for the glacier dynamics. J. Glaciol. 56, 781–794.

Nick, F.M., et al., 2013. Future sea-level rise from Greenland's main outlet glaciers in a warming climate. Nature 497, 235–238.

Nowicki, S., et al., 2013. Insights into spatial sensitivities of ice mass response to environmental change from the SeaRISE ice sheet modeling project I: Antarctica. J. Geophys. Res., Earth Surf. 118, 1002–1024.

Nye, J.F., 1957. The distribution of stress and velocity in glaciers and ice-sheets. Proc. R. Soc. Lond. Ser. A, Math. Phys. Sci. 239, 113–133.

Oerlemans, J., 2002. On glacial inception and orography. Quat. Int. 95–96, 5–10.

O'Leary, M.J., et al., 2013. Ice sheet collapse following a prolonged period of stable sea level during the last interglacial. Nat. Geosci. 6, 796–800.

Pagani, M., Zachos, J.C., Freeman, K.H., Tipple, B., Boharty, S., 2005. Marked decline in atmospheric carbon dioxide concentrations during the Paleogene. Science 309, 600–603.

Pal, J., et al., 2007. Regional climate modeling for the developing world: the ICTP RegCM3 and RegCNET. Bull. Am. Meteorol. Soc. 88, 1395–1409.

Parizek, B.R., Alley, R.B., Dupont, T.K., Walker, R.T., Anandakrishnan, S., 2010. Effect of orbital-scale climate cycling and meltwater drainage on ice sheet grounding line migration. J. Geophys. Res. 115, F01011.

Patterson, M.O., et al., 2014. Orbital forcing of the East Antarctic ice sheet during the Pliocene and Early Pleistocene. Nat. Geosci. 7, 841–847.

Pattyn, F., et al., 2013. Grounding-line migration in plan-view marine ice-sheet models: results of the ice2sea MISMIP3d intercomparison. J. Glaciol. 59, 410–422.

Pfeffer, W.T., Harper, J.T., O'Neel, S., 2008. Kinematic constraints on glacier contributions to 21st-century sea-level rise. Science 321, 1340–1343.

Pollard, D., DeConto, R.M., 2005. Hysteresis in Cenozoic Antarctic ice sheet variations. Glob. Planet. Change 45, 9–21.

Pollard, D., DeConto, R.M., 2009. Modelling West Antarctic ice sheet growth and collapse through the past five million years. Nature 458, 329–332.

Pollard, D., DeConto, R.M., 2012. Description of a hybrid ice sheet-shelf model, and application to Antarctica. Geosci. Model Dev. 5, 1273–1295.

Pusz, A.E., Thunell, R.C., Miller, K.G., 2011. Deep water temperature, carbonate ion, and ice volume changes across the Eocene–Oligocene climate transition. Paleoceanography 26, PA2205.
Raymo, M.E., Mitrovica, J.X., 2012. Collapse of polar ice sheets during the stage 11 interglacial. Nature 483, 453–456.
Reeh, N., 1968. On the calving of ice from floating glaciers and ice shelves. J. Glaciol. 7, 215–232.
Rignot, E., Jacobs, S., Mouginot, J., Scheuchl, B., 2013. Ice-shelf melting around Antarctica. Science 341, 266–270.
Ritz, C., Rommelaere, V., Dumas, C., 2001. Modeling the evolution of Antarctic ice sheet over the last 420,000 years: implications for altitude changes in the Vostok region. J. Geophys. Res. 106 (D23), 31943–31964.
Roberts, J.L., et al., 2011. Refined broad-band sub-glacial morphology of Aurora Subglacial Basin, East Antarctica derived by an ice-dynamics-based interpolation scheme. The Cryo. 5, 551–560.
Rovere, A., et al., 2014. The Mid-Pliocene sea-level conundrum: glacial isostasy, eustasy and dynamic topography. Earth Planet. Sci. Lett. 387, 27–33.
Rowley, D.B., Forte, A.M., Moucha, R., Mitrovica, J.X., Simmons, N.A., Grand, S.P., 2013. Dynamic topography change of the eastern United States since 3 million years ago. Science 340, 1560–1563.
Scambos, T., Hulbe, C., Fahnestock, M., 2003. Climate-induced ice shelf disintegration in the Antarctic Peninsula. In: Domack, E., et al. (Eds.), Antarctic Peninsula Climate Variability: Historical and Paleoenvironmental Perspectives. In: Antarctic Research Series, vol. 79. American Geophysical Union, pp. 79–92.
Scambos, T.A., Berthier, E., Shuman, C.A., 2011. The triggering of subglacial lake drainage during rapid glacier drawdown: Crane Glacier, Antarctic Peninsula. Ann. Glaciol. 52, 74–82.
Schoof, C., 2007. Ice sheet grounding line dynamics: steady states, stability, and hysteresis. J. Geophys. Res., Earth Surf. 112, F03S28.
Tedesco, M., Monaghan, A.J., 2009. An updated Antarctic melt record through 2009 and its linkages to high-latitude and tropical climate variability. Geophys. Res. Lett. 36, L18502.
Vaughan, D.G., 2008. West Antarctic Ice Sheet collapse: the fall and rise of a paradigm. Clim. Change 91, 65–79.
Vizcaino, M., Mikolajewicz, U., Jungclaus, J., Schurgers, G., 2010. Climate modification by future ice sheet changes and consequences for mass balance. Clim. Dyn. 34, 301–324.
Vogel, S., Fraser, A.D., Heil, P., Galton-Fenzi, B., Alexander, D., 2013. Ice dolines in East Antarctica – ice–ocean interactions from surface melt water drainage events. In: Davos Atmosphere and Cryosphere Assembly DACA-13. Davos, Switzerland, July 8–12, 2013. Abstract 553.
Weertman, J., 1974. Stability of the junction of an ice sheet and an ice shelf. J. Glaciol. 13, 3–11.
Williams, T., et al., 2010. Evidence for iceberg armadas from East Antarctica in the Southern Ocean during the late Miocene and early Pliocene. Earth Planet. Sci. Lett. 290, 351–361.
Young, D.A., et al., 2011. A dynamic early East Antarctic Ice Sheet suggested by ice-covered fjord landscapes. Nature 474, 72–75.